Status of Searches for Magnetic Monopoles*

L. Patrizii[1] and M. Spurio[1,2]

[1]Istituto Nazionale di Fisica Nucleare, Sezione di Bologna, 40127 Bologna, Italy
[2]Dipartimento di Fisica e Astronomia, Università di Bologna, 40127 Bologna, Italy

Annu. Rev. Nucl. Part. Sci. 2015. 65:279–302

First published online as a Review in Advance on June 24, 2015

The *Annual Review of Nuclear and Particle Science* is online at nucl.annualreviews.org

This article's doi:
10.1146/annurev-nucl-102014-022137

*This review is dedicated to the memory of Giorgio Giacomelli, who devoted much of his scientific activity to the study of magnetic monopoles.

Keywords

magnetic monopoles, dyons, proton decay catalysis, accelerator searches, cosmic-ray searches

Abstract

Searches for magnetic monopoles ($\mathcal{M}$s) are a fascinating interdisciplinary area with implications for fundamental theories, particle physics, astrophysics, and cosmology. The quantum theory of $\mathcal{M}$s, and its consistency with electrodynamics, was originally derived by Dirac, marking the beginning of the search for classical monopoles at every new accelerator, including the Large Hadron Collider. $\mathcal{M}$s are required by Grand Unification Theories (GUTs), but unlike classical monopoles they would be incredibly massive, out of reach for any conceivable accelerator. Significant effort has been made to search for $\mathcal{M}$s in the cosmic radiation as relic particles from the early Universe in the widest experimentally available range of mass and velocity. In this review, we discuss the status of the searches for classical $\mathcal{M}$s at accelerators for GUTs, superheavy $\mathcal{M}$s in the penetrating cosmic radiation, and intermediate-mass $\mathcal{M}$s at high altitudes, emphasizing the most recent results and future perspectives.

Contents

1. INTRODUCTION

The concept of the magnetic monopole ($\mathcal{M}$) was introduced by Dirac (1) in 1931 to explain the quantization of the electric charge. Dirac established the basic relation between the elementary electric charge e and the magnetic charge g:

$$\frac{eg}{c} = \frac{n\hbar}{2} \rightarrow g = n \cdot g_D = n \cdot \frac{1}{2}\frac{\hbar c}{e} \sim n \cdot \frac{137}{2}e, \qquad 1.$$

where g_D is the unit Dirac charge and n is an integer. The existence of magnetic charges and currents would symmetrize the Maxwell equations. The symmetry would not be perfect, because the unit magnetic charge is much larger than the electric one. Equation 1 defines most of the properties of Dirac (or classical) $\mathcal{M}$s, as they are assumed to be pointlike particles.

Around 1974, researchers realized (2, 3) that the electric charge is naturally quantized in Grand Unification Theories (GUTs) of the strong and electroweak (EW) interactions. $\mathcal{M}$s appear at the phase transition corresponding to the spontaneous breaking of the unified group into subgroups, one of which is $U(1)$, which describes electromagnetism. In a sense, the situation was the reverse of that reasoned by Dirac: The quantization of the electric charge now implied the existence of $\mathcal{M}$s.

In the context of GUTs, the lowest $\mathcal{M}$ mass, M, is related to the mass of the X vector boson ($m_X \sim 10^{15}$ GeV), which is the carrier of the unified interaction and defines the unification scale

$M \gtrsim m_X/\alpha \simeq 10^{17}$ GeV, where $\alpha \simeq 0.025$ is the dimensionless unified coupling constant [natural units with $c = 1$ in the centimeter-gram-second (c.g.s.) system of units are almost always used in this review]. Larger $\mathcal{M}$ masses are expected if gravity is brought into the unification picture, as well as in some supersymmetric models. $\mathcal{M}$s with $M \sim 10^5 \div 10^{12}$ GeV [also called intermediate-mass monopoles (IM$\mathcal{M}$s)] are predicted by theories with an intermediate energy scale between the GUT and the EW scales and would appear in the early Universe at a considerably later time than the GUT epoch (4). The lowest-mass $\mathcal{M}$ is stable because magnetic charge, like electric charge, is conserved.

The possibility that the gauge theory of EW interactions allows $\mathcal{M}$ solutions (also with multiple magnetic charge) has been realized (5, 6). With a basic magnetic charge that is twice the Dirac charge ($g = 2g_D$), such a $\mathcal{M}$ can be interpreted as a nontrivial hybrid between the Dirac and the GUT (electrically charged) monopoles. The mass of this $\mathcal{M}$ has been estimated to range between 3 and 7 TeV (7), making it a very good candidate for searches at the CERN Large Hadron Collider (LHC).

In this review, we discuss the status and perspectives of the searches for $\mathcal{M}$s. The theoretical motivations for Dirac and GUT $\mathcal{M}$s have been extensively covered elsewhere (8), so we discuss this topic only briefly in Section 2. An exhaustive review of the phenomenology of $\mathcal{M}$s and of the early searches is also available (9), as are recent reviews of the different monopole models (10, 11). In Section 3, we discuss the interactions between $\mathcal{M}$s and matter, as well as their energy loss mechanisms, and in Section 4 we present the most common experimental techniques for their detection. The status of the searches for $\mathcal{M}$s in the cosmic radiation and at accelerators is discussed in Section 5. Finally, we present perspectives for ongoing and future experiments in Section 6.

2. CLASSICAL, GRAND UNIFICATION THEORY, AND INTERMEDIATE-MASS MAGNETIC MONOPOLES

No predictions for the Dirac monopole mass (M_D) exist. A general assumption has been that the classical electron radius is equal to the so-called classical monopole radius, from which one obtains $M_D \sim g_D^2 m_e/e^2 \sim 4{,}700\, m_e \sim 2.4$ GeV. On the basis of this assumption, searches have been performed for classical $\mathcal{M}$s at every new accelerator.

At accelerators, $\mathcal{M}$s can be produced via electromagnetic processes similar to those involving the creation of electrically charged fermion pairs through a dimensionless magnetic constant, α_m, that depends on the magnetic unit charge, g_D. This constant may be introduced in analogy with the fine-structure constant $\alpha = e^2/\hbar c \simeq 1/137$, and it corresponds to $\alpha_m = g_D^2/\hbar c \simeq 34.25$. Therefore, the electromagnetic interactions of $\mathcal{M}$s are too strong for perturbative theory to be applicable. A quantitative estimate of the production cross sections cannot be reliably derived, which remains an open problem.

GUT $\mathcal{M}$s and IM$\mathcal{M}$s are expected to be very massive composite objects, well beyond the reach of any existing or foreseen accelerator. Such poles could have been produced in the early Universe (12) as a component of cold dark matter and could still exist as cosmic relics. Their kinetic energy would have been affected by the expansion of the Universe and by traveling through the galactic and intergalactic magnetic fields.

2.1. History of Grand Unification Theory Magnetic Monopoles

In the standard Big Bang model, the Universe started in a state of extremely high density and temperature. As time progressed, density and temperature decreased and the particle composition of the Universe changed. The grand unification of strong and EW interactions lasted until the

temperature dropped to $\sim 10^{15}$ GeV, when a phase transition is thought to have occurred. During that phase transition, GUT monopoles appeared as topological defects, approximately one pole for each causal domain. This situation would lead to a present-day abundance of $\mathcal{M}$s (13), exceeding by many orders of magnitude the critical energy density of the Universe (14):

$$\rho_c \equiv \frac{3H^2}{8\pi G_N} = 1.88 \cdot 10^{-29} h^2 (\mathrm{g\,cm^{-3}}) = 1.05 \cdot 10^{-5} h^2 (\mathrm{GeV\,cm^{-3}}), \qquad 2.$$

where the scaled Hubble parameter ($h \sim 0.7$) is defined in terms of the Hubble constant $H \equiv 100h$ km s^{-1} Mpc^{-1}. This overabundance has been called the magnetic monopole problem. Cosmological inflation would lead to a present-day abundance of $\mathcal{M}$s that is significantly smaller than could plausibly be detected. The reduction of $\mathcal{M}$s in the Universe was one of the motivating factors for cosmological inflation (15). Observable abundances can be obtained in scenarios with carefully tuned parameters or scenarios in which the reheating temperature is large enough to allow $\mathcal{M}$ production in high-energy collisions between fermions (fs), such as $f\bar{f} \to \mathcal{M}\bar{\mathcal{M}}$.

As the Universe expanded and cooled down, the energy of $\mathcal{M}$s decreased for the adiabatic energy loss, like any other particle or type of radiation. $\mathcal{M}$s would have reached a speed of $\beta \sim 10^{-10}$ during the epoch of galaxy formation. As matter (including $\mathcal{M}$s and dark matter) started to condense gravitationally into galaxies, galactic magnetic fields developed through the dynamo mechanism. $\mathcal{M}$s were accelerated by these magnetic fields, and after a time on the order of 10^7 years, they could be ejected with velocities of $\beta \sim (1 \div 3) \times 10^{-2}$. This process would have given rise to an isotropic intergalactic flux of relatively high energy $\mathcal{M}$s.

Today, we may expect a sizable fraction of monopoles bound to different systems, such as the local galaxy cluster, our Galaxy, or the Solar System. In the absence of magnetic fields, $\mathcal{M}$s have velocities comparable to the virial velocity of objects gravitationally bound to the system. There may be peaks in the velocity spectrum corresponding to poles bound to the Sun ($\beta \sim 10^{-4}$), to the Galaxy ($\beta \sim 10^{-3}$), or to the local galaxy cluster ($\beta \gtrsim 10^{-2}$). These gravitationally bound $\mathcal{M}$s could produce a flux on Earth.

A magnetic field $\mathbf{B}$ acting over a length ℓ increases the kinetic energy of a monopole by a quantity $gB\ell$. The speed a $\mathcal{M}$ can reach in a typical galactic magnetic field of strength $B \sim 3 \times 10^{-6}$ G and a coherent length $\ell \sim 300\,\mathrm{pc} = 10^{21}$ cm depends on its mass M:

$$\beta \simeq \begin{cases} c & M \lesssim 10^{11}\,\mathrm{GeV} \\ 10^{-3} \left(\frac{10^{17}\,\mathrm{GeV}}{M}\right)^{1/2} & M \gtrsim 10^{11}\,\mathrm{GeV}. \end{cases} \qquad 3.$$

From the experimental point of view, classical cosmic monopoles are expected to be relativistic, whereas GUT monopoles can have speeds over a wide range.

IM$\mathcal{M}$s would also survive as relics of the early Universe (16) and be stable. Because IM$\mathcal{M}$s would be produced after inflation, their number would not be reduced by inflationary mechanisms. IM$\mathcal{M}$s with $10^7 < M < 10^{12}$ GeV could acquire nearly relativistic velocities in one coherent domain of the galactic field (17). Experimentally, one has to look for IM$\mathcal{M}$s with $\beta \gtrsim 0.1$.

2.1.1. Structure of a Grand Unification Theory magnetic monopole. The central core of a GUT $\mathcal{M}$ retains the original symmetry and contains the fields of the superheavy gauge bosons, which mediate baryon number violation. Through these bosons, the strong and EW interactions between particles are indistinguishable: In this domain, quarks and leptons are the same particles. The $\mathcal{M}$'s core should be surrounded by a fermion–antifermion condensate, which would have baryon number–violating terms (see Section 2.1.3) extending up to the confinement region.

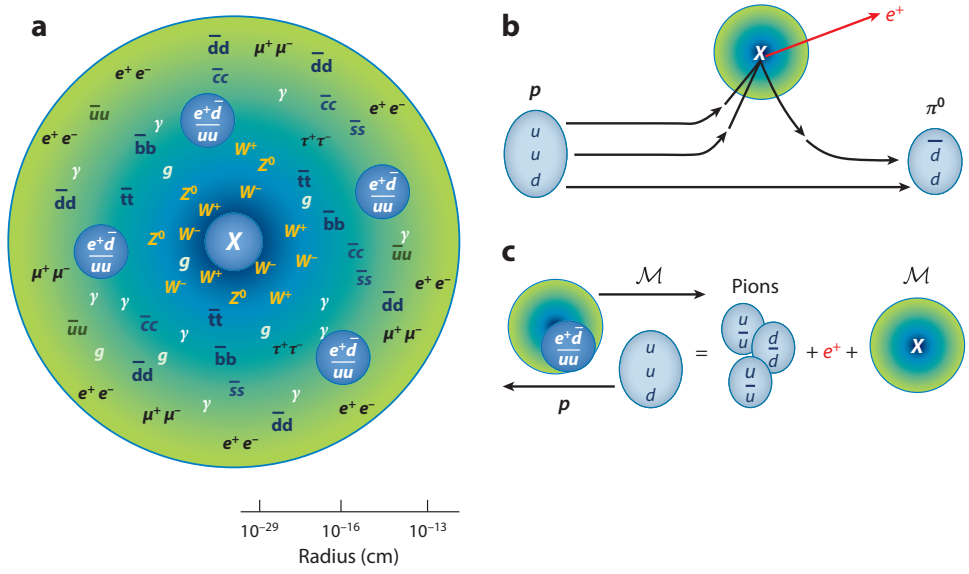

Figure 1

(*a*) The GUT monopole structure. The various regions correspond to the following: Grand Unification ($r \sim 10^{-29}$ cm). Inside this core, virtual X bosons should be present. The electroweak unification region ($r \sim 10^{-16}$ cm) contains virtual $W^{\pm}$ and Z^0 bosons. The confinement region ($r \sim 10^{-13}$ cm) contains virtual photons, gluons, a fermion–antifermion condensate, and four-fermion bags. For radii larger than a few femtometers, one has the field of a point magnetic charge $B = g/r^2$. (*b*) The monopole catalysis of proton decay through the reaction $p + \mathcal{M} \rightarrow \mathcal{M} + e^+ + \pi^0$. (*c*) The effect of the presence of a four-fermion condensate, $\overline{uud}e^+$, that can induce proton decay.

Figure 1 shows the structure of a GUT $\mathcal{M}$. It has very small core, an EW region, a confinement region, and a fermion–antifermion condensate (which may contain four-fermion agglomerates that induce baryon number–violating processes). For $r \geq 3$ fm, a GUT $\mathcal{M}$ behaves as a point particle generating a field $B = g/r^2$.

IM$\mathcal{M}$s produced after the decoupling of the strong and EW interactions would have a structure similar to that of a GUT $\mathcal{M}$. The core radius would be larger (because $R \sim 1/M$), and the outer cloud would not contain terms that allow baryon number violation.

2.1.2. Dyons. A dyon is a particle carrying both electric and magnetic charges. Therefore, when at rest, it produces both electrostatic and magnetostatic fields. For two dyons, one with charges e_1 and g_1 and the other with e_2 and g_2, the Dirac quantization condition becomes $e_1 g_2 - e_2 g_1 = (\hbar c/2)n$. Semiclassical arguments have been used to suggest that in a proper quantum-mechanical treatment the dyon charge must be quantized. In the GUT framework, quantum fluctuations lead to a quantized electric charge of the dyon in integer multiples of the minimal electric charge (18).

A $\mathcal{M}$ and a proton may form a bound system with both magnetic and electric charges (19). As far as the energy loss in matter is concerned, a positively charged dyon and an ($\mathcal{M} + p$)-bound system behave in the same way.

2.1.3. Magnetic monopole catalysis of nucleon decay. As early as 1980, researchers hypothesized that, given its inner structure, a GUT $\mathcal{M}$ could catalyze baryon number–violating processes such as $p + \mathcal{M} \rightarrow \mathcal{M} + e^+ +$ mesons. The cross section of this process (σ_0) would be

incredibly small if it were on the order of the geometrical dimension of the $\mathcal{M}$ core ($\sim 10^{-58}$ cm^2). If the interaction is independent of m_X, then σ_0 could be comparable to that of ordinary strong interactions, the so-called Rubakov–Callan mechanisms (20, 21). This possibility has important implications both in particle physics and in astrophysics. The catalysis reaction on the $\mathcal{M}$ core can be depicted as in **Figure 1*b***, whereas the effect of the presence of a condensate of four fermions ($\overline{uud}e^+$) is illustrated in **Figure 1*c***.

The cross section for the catalysis of nucleon decay ($\sigma_{\rm cat}$) depends not only on the cross section σ_0 but also on the monopole speed as $\sigma_{\rm cat} = (\sigma_0/\beta) \cdot F(\beta)$. The correction factor $F(\beta)$ takes into account an additional angular momentum of the monopole–nucleus system and becomes relevant for speeds below a threshold β_0, which depends on the nucleus (22). For speeds above β_0, $F(\beta) = 1$.

Positively charged dyons, or $(\mathcal{M} + p)$ states, should not catalyze proton decay with large rates because of the electrostatic repulsion between the protons and the dyons. Negatively charged dyons would instead have large effective cross sections.

2.2. Cosmological and Astrophysical Bounds on Grand Unification Theory Monopoles

Different upper limits on the flux of cosmic $\mathcal{M}$s have been obtained on the basis of cosmological and astrophysical considerations. Most of these bounds must be considered rough orders of magnitude only. One obtains a simple cosmological bound by requiring that the present monopole mass density (ρ_M) be smaller than the critical density given in Equation 2: $\rho_M = n_M M < \rho_c$. Correspondingly, for the $\mathcal{M}$ number density one should have $n_M < \rho_c/M$. The $\mathcal{M}$ flux per unit solid angle (Φ_M) is simply related to the number density (n_M) and to the $\mathcal{M}$s' average speed, $v = c\beta$, in the observed frame

$$\Phi_M = \frac{n_M v}{4\pi} < \frac{\rho_c c}{4\pi} \cdot \frac{\beta}{M} \simeq 2.5 \cdot 10^{-13} h^2 \cdot \frac{\beta}{(M/10^{17}\ \mathrm{GeV})} (\mathrm{cm}^{-2}\mathrm{s}^{-1}\mathrm{sr}^{-1}). \quad 4.$$

The limit holds in the hypothesis of poles uniformly distributed in the Universe.

A more stringent limit for most of the (M, β) parameter space can be derived by astrophysical considerations. Most celestial bodies possess large-scale magnetic fields. In our Galaxy, the magnetic field is stretched in the azimuthal direction along the spiral arms, and it likely originated from the nonuniform rotation of the Galaxy. The timescale of this generation mechanism is approximately equal to the rotation period of the Galaxy: $\tau_B \sim 10^8$ years. Magnetic poles would gain energy, which is taken from the stored magnetic energy. One can obtain an upper bound for the $\mathcal{M}$ flux by requiring that the kinetic energy gained per unit time be at most equal to the magnetic energy generated by the dynamo effect. The rate of energy, $\mathrm{d}E_M/\mathrm{d}t$, acquired per unit volume V by $\mathcal{M}$s in a magnetic field $\mathbf{B}$ is

$$\frac{\mathrm{d}E_M}{\mathrm{d}t\mathrm{d}V} = \mathbf{J}_M \cdot \mathbf{B}\ (\mathrm{erg\,s^{-1}\,cm^{-3}}), \quad 5.$$

where the magnetic current density is $\mathbf{J}_M = g n_M \mathbf{v}$ and $\mathbf{v}$ is the average pole velocity. The magnetic energy density generated by the dynamo effect per unit time yields

$$\frac{\mathrm{d}E_D}{\mathrm{d}t\mathrm{d}V} = \frac{\rho_B}{\tau_B} = \frac{B^2}{8\pi\tau_B} (\mathrm{erg\,s^{-1}cm^{-3}}), \quad 6.$$

where $\rho_B = B^2/8\pi$ is the energy density of the magnetic field $\mathbf{B}$. Assuming that $\mathbf{v}$ and $\mathbf{B}$ are parallel over large distances, the condition $\mathbf{J}_M \cdot \mathbf{B} < B^2/8\pi\tau_B$ leads to the following upper bound:

$n_M < B/(8\pi\tau_B g v)$. As in Equation 4, one can obtain a relation between flux and number density,

$$\Phi_M = \frac{n_M v}{4\pi} \lesssim \frac{B}{32\pi^2 \tau_B g} \simeq 10^{-16}\,(\mathrm{cm}^{-2}\,\mathrm{s}^{-1}\,\mathrm{sr}^{-1}), \qquad 7.$$

for the typical value of the Galactic magnetic field strength, $B \sim 3 \times 10^{-6}$ G, and single Dirac charge, $g = g_D$. This is the so-called Parker bound (23). Note that the condition in Equation 7 is always more stringent than that in Equation 4 for $M < 10^{17}$ GeV and $\beta > 10^{-3}$.

In a more detailed treatment (24), which assumes reasonable choices for the astrophysical parameters and a random relation between **v** and **B**, the $\mathcal{M}$s would acquire lower energies. Correspondingly, less energy is removed from the Galactic field, and the Parker bound is less restrictive. In different speed regimes (indicated in Equation 3) and with critical speed defined as $\beta_c = 10^{-3}$, the upper bounds (24) are

$$\Phi_M \lesssim \begin{cases} 10^{-15}\,(\mathrm{cm}^{-2}\,\mathrm{s}^{-1}\,\mathrm{sr}^{-1}), & M \lesssim 10^{17}\ \mathrm{GeV}, \\ 10^{-15}\left(\frac{10^{17}\mathrm{GeV}}{M}\right)\left(\frac{\beta}{\beta_c}\right)(\mathrm{cm}^{-2}\,\mathrm{s}^{-1}\,\mathrm{sr}^{-1}), & M \gtrsim 10^{17}\,\mathrm{GeV}. \end{cases} \qquad 8.$$

An extended Parker bound, obtained by considering the survival of an early seed field (25, 26), yields a tighter bound:

$$\Phi_M \lesssim 1.2 \cdot 10^{-16}\left(\frac{M}{10^{17}\,\mathrm{GeV}}\right)(\mathrm{cm}^{-2}\,\mathrm{s}^{-1}\,\mathrm{sr}^{-1}). \qquad 9.$$

3. MAGNETIC MONOPOLE ENERGY LOSSES

It is important to study $\mathcal{M}$s' interactions in order to understand the stopping power mechanisms in matter in general and the energy losses in particle detectors in particular. The long-range interaction between a $\mathcal{M}$ and a fermion, an atomic system, or a nucleus is due to the "magnetostatic" interaction between the field, $\mathbf{B_M}$, of the pole magnetic charge and the magnetic dipole moment, $\boldsymbol{\mu}$, of the fermion, atom, or nucleus (19, 27). The interaction energy arising from the magnetic charge–magnetic dipole interaction is given by

$$W_D = -\boldsymbol{\mu} \cdot \mathbf{B_M}, \qquad 10.$$

which, for an electron, corresponds to $W_D = \hbar^2/4m_e r^2$. If one assumes a relative distance equal to the Bohr radius, $r = a_o = 0.53 \times 10^{-8}$ cm, then $W_D \simeq 7$ eV, which is comparable to the binding energy of an atom. Thus, one expects a sizable deformation of an atom when a $\mathcal{M}$ passes inside or close to an atomic system. For a proton at a distance of $r = 1$ fm from the monopole, $W_D \sim 30$ MeV, which is larger than the binding energy of nucleons in nuclei. Thus, one expects deformations of the nucleus when a monopole passes close to it.

Classical and light ($M < 10^{11}$ GeV) cosmic $\mathcal{M}$s are expected (Equation 3) to have relativistic velocities and huge energy losses, more than enough for them to be easily detected. Furthermore, their energy loss would be sufficiently large to stop a considerable fraction of monopoles crossing the Earth. Therefore, searches for monopoles trapped in the Earth are particularly important. GUT $\mathcal{M}$s have such large masses that it is difficult to accelerate them to large velocities, and the study of the energy loss of slow-moving $\mathcal{M}$s is relevant for their detection.

3.1. Stopping Power of Fast Monopoles with $\beta > 0.05$

A moving $\mathcal{M}$ produces an electric field whose lines of force lie in a plane perpendicular to the monopole trajectory. In matter, this field may ionize or excite the nearby atoms or molecules. The

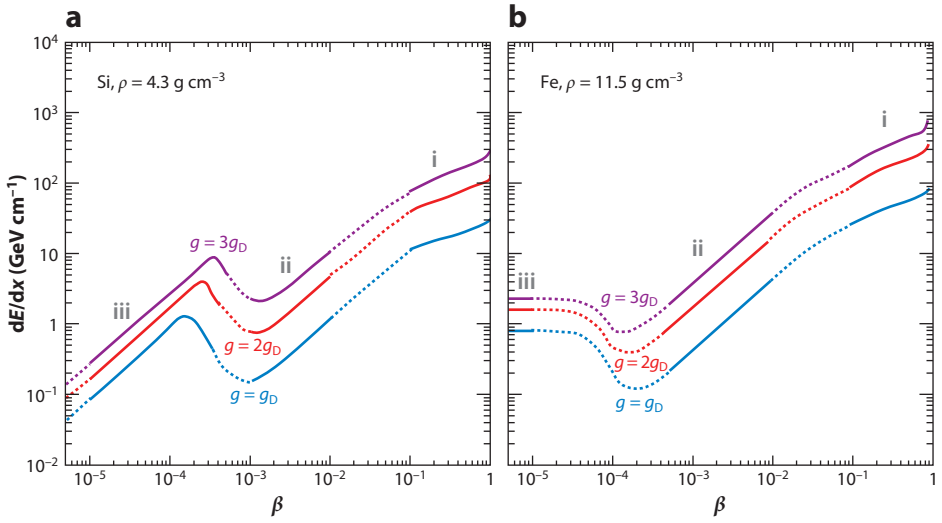

Figure 2

Energy losses of $\mathcal{M}$s (*a*) in the Earth's mantle and (*b*) in the Earth's nucleus as function of velocity β for different values of the magnetic charge g. The solid curves in the regions labeled *i*, *ii*, and *iii* indicate that the calculations are more reliable, and the dashed lines show where they are interpolated. The three curves apply to $\mathcal{M}$s with $n = 1, 2$, or 3 unit Dirac charge and assuming that the basic electric charge is that of the electron. The curves labeled $g = 3g_D$ also apply to $\mathcal{M}$s with $g = g_D$ if the basic electric charge is that of the *d* quark. Each curve in the region labeled *iii* shows the stopping power in the Earth's mantle and nucleus for slowly moving $\mathcal{M}$s. Each curve in the region labeled *i* is computed according to Equation 11.

interaction between $\mathcal{M}$s with velocities $\beta > 0.05$ and $\gamma \leq 100$ and the electrons of a material is well understood. The ionization energy loss for electric charges (see the section titled Passage of Particles Through Matter of Reference 14) can be adapted for a magnetic charge (28) by replacing $Ze \rightarrow g\beta$. The stopping power then becomes

$$\frac{dE}{dx} = \frac{4\pi N_e g^2 e^2}{m_e c^2}\left[\ln\left(\frac{2m_e c^2 \beta^2 \gamma^2}{I}\right) - \frac{1}{2} + \frac{k}{2} - \frac{\delta}{2} - B_m\right], \qquad 11.$$

where N_e is the density of electrons, m_e is the electron mass, I is the mean ionization potential of the crossed medium, δ is the density effect correction, k is the QED correction, and B_m is the Bloch correction (refer to Reference 29 for the numerical values for different materials). In practice, in this velocity range a $\mathcal{M}$ with magnetic charge g_D behaves as an equivalent electric charge: $(Z)^2 = g_D^2\beta^2 \sim (68.5\beta)^2$. This energy loss mechanism is implemented as part of a GEANT package (30) for the simulation of monopole trajectories in a detector (31). **Figure 2** shows the $\mathcal{M}$ stopping power in silicon at the density of the Earth's mantle and in iron at the density of the Earth's core.

When $\beta\gamma > 10^4$, stochastic processes such as bremsstrahlung, pair production, and hadron production dominate the energy loss. Photonuclear processes yield the largest contribution in materials with moderate atomic mass (such as rock or water), with a smaller contribution from pair production. In contrast, pair production is the dominant process in materials with high atomic number Z. The contribution from bremsstrahlung is small and is usually neglected. Theoretical uncertainties arising from the large coupling constant α_m should be considered in the computation of transition probabilities. Thus, the energy loss per unit path length in this energy regime is

dominated by single (or small numbers of) collisions with the possibility of a large energy transfer, leading to large fluctuations on the stopping power and range of the particle.

3.2. Stopping Power of Monopoles with $10^{-3} \lesssim \beta \lesssim 10^{-2}$

The velocity range $10^{-3} \lesssim \beta \lesssim 10^{-2}$ is of particular interest because of the considerations described in Section 2.1 for massive $\mathcal{M}$s bound to astrophysical systems. In calculations of the energy loss, the material is approximated by a free (degenerate) gas of electrons. This approximation is appropriate in the description of $\mathcal{M}$s' interactions with the conduction electrons of metallic absorbers. For nonmetallic absorbers, it is a reasonable approximation for heavy atoms ($Z \geq 10$). Using this approximation, Ahlen & Kinoshita (32) computed the stopping power in the velocity range $10^{-3} \lesssim \beta \lesssim 10^{-2}$ as

$$\frac{\mathrm{d}E}{\mathrm{d}x} = \frac{2\pi N_e g^2 e^2 \beta}{m_e c v_\mathrm{F}} \left[\ln \frac{2 m_e v_\mathrm{F} a_o}{\hbar} - \frac{1}{2} \right], \qquad 12.$$

where $v_\mathrm{F} = (\hbar/m_e)(3\pi^2 N_e)^{1/3} \simeq 3.9 \times 10^8$ cm s^{-1} is the Fermi velocity (the value applies to silicon at the Earth's mantle density, $\rho_\mathrm{Si} = 4.3$ g cm^{-3}), a_o is the Bohr radius, and N_e is the density of electrons.

The expected $\mathcal{M}$'s energy loss is larger than that computed with Equation 12 if the contribution from the coupling of the $\mathcal{M}$ with the electron magnetic moment is considered. Doing so yields a multiplicative factor of 1.37 to Equation 12 (32). For conductors, one should add another term that depends on the conduction electrons. **Figure 2** depicts the expected stopping power of $\mathcal{M}$ in the Earth's mantle and core for $10^{-3} \lesssim \beta \lesssim 10^{-2}$.

Note that the stopping power mechanism parameterized with Equation 12 refers to an average energy transferred to atomic electrons, which is so small that it is impossible to disregard the electrons' atomic bindings. In addition, transitions yielding photons in the visible range are largely suppressed. For this reason, Equation 12 cannot be used directly to evaluate the response of excitation- and ionization-sensitive particle detectors to slow, supermassive $\mathcal{M}$s (32).

3.3. Stopping Power of Monopoles with $\beta \lesssim 10^{-3}$

In the velocity range $\beta \lesssim 10^{-3}$, $\mathcal{M}$s cannot excite atoms, but they can lose energy in elastic collisions with atoms or nuclei through their coupling with the atomic or nuclear magnetic moment. Different computations have been performed for diamagnetic and paramagnetic materials (29).

At low velocities, the energy loss is released mainly to the medium in the form of thermal and acoustic energy. Particle detectors are sensitive to $\mathcal{M}$s only through particular interaction mechanisms, such as the Drell effect (see Section 4.3), and via atomic recoils.

3.4. Range of Magnetic Monopoles

$\mathcal{M}$s can cross the atmosphere and reach underground detectors, depending on their stopping power, which in turn depends on the monopole mass M and velocity. One can compute the range R by integrating the stopping power:

$$R = \int_{E_\mathrm{min}}^{E_0} \frac{\mathrm{d}E}{\mathrm{d}E/\mathrm{d}x}. \qquad 13.$$

Here, E_0 is the pole initial kinetic energy and E_min is the kinetic energy corresponding to $\beta \simeq 10^{-6}$, when the $\mathcal{M}$ can be considered stopped. **Figure 3** shows the ratio R/M (in g cm^{-2} GeV^{-1}) as a

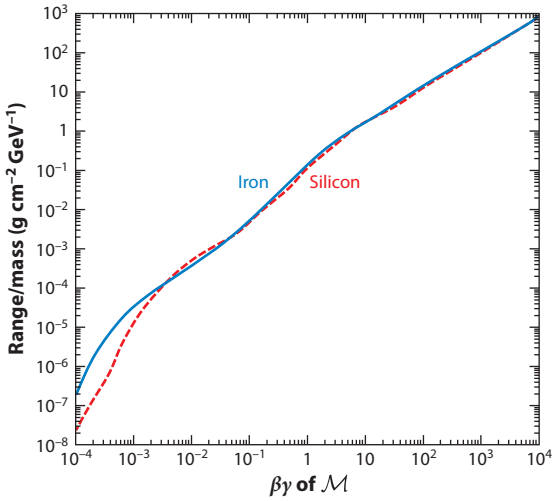

Figure 3

The ratio of range to mass for $\mathcal{M}$s with unit Dirac charge in iron and silicon as a function of monopole $\beta\gamma = p/M$. The range is computed from the stopping powers given in Reference 29 and defined as the thickness of the material needed to slow down the monopole to $\beta = 10^{-6}$.

function of the initial $\beta\gamma = p/M$ of the $\mathcal{M}$, where p is the $\mathcal{M}$'s momentum (33). The stopping power used in the computation is that obtained in silicon and iron in Reference 29.

Because the range depends on the kinetic energy, the R/M ratio is independent of the mass. From **Figure 3**, we can estimate that the minimum mass required for, say, a $\beta = 10^{-3}$ $\mathcal{M}$ to cross the Earth's atmosphere (1,000 g cm^{-2}) is $M \simeq 3 \times 10^{7}$ GeV. The mass increases to approximately $M \simeq 10^{10}$ GeV for a monopole penetrating 3×10^{5} g cm^{-2}, corresponding to the minimum rock overburden of the Gran Sasso laboratory in Italy.

4. EXPERIMENTAL METHODS FOR MAGNETIC MONOPOLE SEARCHES

Search strategies for $\mathcal{M}$s are determined by their expected interactions as they pass through a detector. Searches in cosmic rays, in matter, and at accelerator experiments are based on different techniques, such as the induction method, which exploits the electromagnetic interaction of the $\mathcal{M}$ with the quantum state of a superconducting ring, or the $\mathcal{M}$'s energy loss in different detectors.

4.1. The Induction Technique in Superconductive Coils

The technique of looking for monopoles by using small superconducting coils was introduced in the mid 1970s (34). The detection method consists of a superconducting coil coupled to a SQUID (superconducting quantum interferometer device). In a superconducting ring, a moving $\mathcal{M}$ induces an electromotive force and a current change (Δi). For a coil with N turns and inductance L, the current change is $\Delta i = 4\pi N n g_{\mathrm{D}}/L = 2\Delta i_o$, where i_o is the current change corresponding to a change of one unit of the flux quantum of superconductivity. This method is based only on the long-range electromagnetic interaction between the magnetic charge and the macroscopic quantum state of a superconducting ring. For any sample of matter containing only magnetic dipoles, induced currents cancel to zero after its passage through the coil. A persistent current directly proportional to g_{D} would represent an unmistakable signature of the $\mathcal{M}$'s passage. Induction coils

are the only known devices that are sensitive only to the magnetic charge, so they are able to detect poles of any velocity and mass. The system components, especially the magnetometer, have to be extremely well shielded from any variation of the ambient magnetic field, placing severe restrictions on the cross-sectional area of induction detectors.

SQUIDs have been used in the past to search for $\mathcal{M}$s in the cosmic radiation. In 1982, a group based at Stanford University operated a four-turn coil with a 5-cm diameter for 151 days (35), recording a single current jump corresponding to that expected from a magnetic charge equal to g_D. No other jumps were observed in subsequent runs. That candidate event generated a great deal of interest in $\mathcal{M}$s, and the induction detection technique evolved quickly toward second-generation experiments. No additional candidates were found. This technique is no longer used to search for $\mathcal{M}$s in the cosmic radiation, but it is still widely used in searches for $\mathcal{M}$s trapped in matter (see Section 5.4).

4.2. Light Yield in Scintillators

Different computations exist for the light yield of $\mathcal{M}$s and dyons in a liquid or plastic scintillator. For a detailed review, see Reference 36. The light yield (dL/dx) in a scintillator is related to the total electronic energy loss (dE/dx) by

$$\frac{dL}{dx} = \mathcal{A} \times \left[\frac{1-F}{1+\mathcal{AB}(1-F)\frac{dE}{dx}} + F \right] \times \frac{dE}{dx}. \qquad 14.$$

For relatively small energy losses, $dL/dx \simeq \mathcal{A} \times dE/dx$, where $\mathcal{A} \simeq 0.03 \div 0.07$, depending on the material and on the $\mathcal{M}$'s velocity. The light yield from the energy deposited near the particle track (the first term in the brackets in Equation 14) saturates for high energy losses. The term $\mathcal{B} = 0.3 \div 0.7$ cm MeV^{-1} is called the quenching parameter. The term F (which is small in most cases) represents the fraction of energy loss that results from excitations outside the track core; these excitations are assumed not to be quenched.

Figure 4*a* shows the results of detailed calculations in a wide range of velocities. Note that at very low velocities the light yield increases with β, then saturates at $\sim$1.2 MeV cm^{-1}. The increase in the light yield is due to changes in the quenching parameter. For $\beta \geq 0.09$, some ionized electrons have sufficient energy to escape from the region near the track core (δ-rays), and the light yield increases again with β. At intermediate β values ($0.003 < \beta < 0.1$), the light yield is almost independent of the magnetic charge g; at low and high β values, the light yield increases as g^2. The light yield at low velocities has to be considered a lower limit, given that the calculations do not take into account possible contributions that can arise from the mixing and crossing of molecular electronic energy levels at the passage of the magnetic charge. The mixing and crossing could result in molecular excitations and emission of additional light.

4.3. Ionization in Gaseous Detectors and the Drell Effect

A gaseous detector [e.g., the drift tubes of the Soudan 2 experiment or the streamer tube subsystem of the Monopole Astrophysics and Cosmic Ray Observatory (MACRO) experiment; see Section 5.2] is characterized by a pressure that approximately corresponds to that of the atmosphere. Thus, the resulting density is very low (in comparison with the density of other detectors), on the order of $\sim 10^{-3}$ g cm^{-3}.

For velocities $\beta > 0.05$, the monopole energy loss in gaseous detectors is well described by Equation 11. The ionization potential of the medium is $\sim$50 eV; **Figure 4*b*** shows the resulting energy losses.

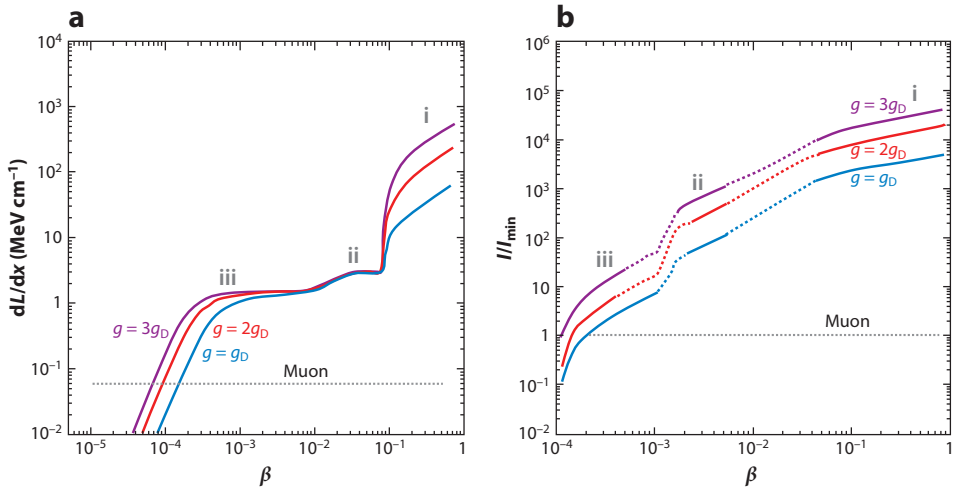

Figure 4

(*a*) Light yield of $\mathcal{M}$s in plastic or liquid scintillators as a function of velocity β for different magnetic charges g. The light yield from a minimum ionizing muon is shown for comparison. At very low velocities the light yield increases with β, then saturates at ~1.2 MeV cm^{-1} (region *iii*). The increase in the light yield (region *ii*) is due to changes in the quenching parameter. For $\beta \geq 0.09$, some ionized electrons have sufficient energy to escape from the region near the track core (δ-rays), and the light yield increases again with β (region *i*). At intermediate β values ($0.003 < \beta < 0.1$) (region *ii*), the light yield is almost independent of g; at low and high β values, the light yield increases as g^2. (*b*) Energy losses produced in the limited streamer tubes filled with 73% helium and 27% *n*-pentane, $\rho = 0.856 \times 10^{-3}$ g cm^{-3}, by $\mathcal{M}$s as a function of β, relative to the ionization produced by a minimum ionizing particle, $I_{min} = 2.2$ MeV g cm^{-2}. The solid curves represent the regions in which the calculations are more reliable; the dashed lines represent interpolated values.

At intermediate velocities, $10^{-3} < \beta < 10^{-2}$, the usual approach is to consider the medium to be a degenerate electron gas (see Section 3.2). At the low densities of a gas, the electrons are not free but rather bound in well-separated molecules. Thus, the assumptions yielding the increase in the light yield in **Figure 4*b*** are affected by larger uncertainties.

At low velocities, $10^{-4} < \beta < 10^{-3}$, and for particular gases such as hydrogen and helium, the Drell effect (37) occurs. Due to the coupling between the pole magnetic field and the electron magnetic moment, the atomic energy levels are changed by the passage of a slowly moving magnetic charge, and an electron can make a transition to an excited level. The energy levels of the atom split in the characteristic Zeeman pattern. The $\mathcal{M}$'s energy loss can be observed in the form of subsequent electromagnetic radiation when the excited electrons return to their ground states. The Drell mechanism is effective as long as the monopole–atom collision energy exceeds the spacing of atomic levels. One may use this effect for practical detection either by observing photons emitted in the deexcitation of atoms or by observing the ionization caused by the energy transfer from the excited atoms to complex molecules with a low ionization potential (the Penning effect). Helium plus *n*-pentane (C_5H_{12}) was used for this purpose in the MACRO streamer tube subsystem (see Section 5.3). **Figure 4*b*** shows the results of calculations (36) performed for different values of the magnetic charge g.

4.4. Energy Loss Mechanisms in Nuclear Track Detectors

The passage of heavily ionizing particles may be permanently recorded as a latent track in some insulating materials known as nuclear track detectors (NTDs), such as polymers, kapton, and

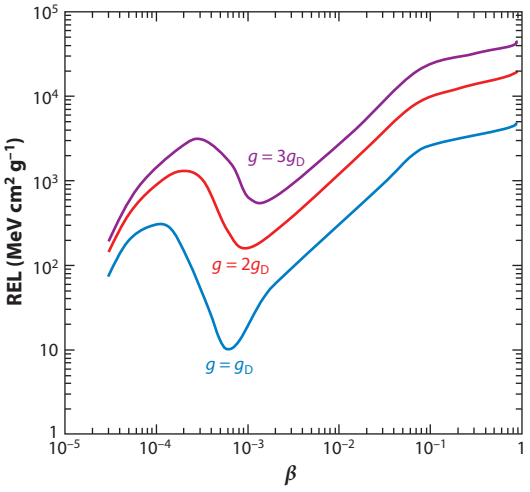

Figure 5

Restricted energy loss (REL) in CR39® as a function of velocity β for $\mathcal{M}$s with magnetic charges $g = g_D$, $2g_D$, and $3g_D$.

nitrocellulose; glasses; and minerals such as mica and obsidian. NTDs are sensitive to the fraction of the energy loss released in a narrow region close to the particle's trajectory. In polymers such as CR39®, Makrofol®, or Lexan™, the restricted energy loss (REL) is the relevant quantity. At high velocities of $\mathcal{M}$ ($\beta > 0.05$), the REL excludes the energy transfers resulting in energetic δ-rays and, thus, in energy being deposited far away from the latent track (38). At lower $\mathcal{M}$ velocities ($\beta < 10^{-2}$), elastic recoils from diamagnetic interactions between the $\mathcal{M}$ and the atoms have to be considered. A detailed computation of these energy loss mechanisms has been performed (36), and **Figure 5** shows the REL in CR39 as a function of β. The atomic elastic recoil contribution gives rise to a bump in the REL below $\beta \sim 10^{-3}$.

The latent track produced by the REL may be visualized under an optical microscope by proper chemical etching (9). NTDs are detection threshold devices, with no time resolution. The threshold depends on the material and on the chemical etching. Chemical etching forms two regular etch-pit cones on each side of the detector sheet along the track of a crossing particle. The REL may be determined from the geometry of the etched cones. For CR39 this technique is particularly successful, yielding measurements of the electric charge of heavy relativistic nuclei ($Z > 5$) to a precision of $0.05e$ if several layers of plastic sheets are used (39, 40).

The CR39 NTD was calibrated with relativistic and low-velocity ($\beta \geq 4 \times 10^{-3}$) ions over the entire range of REL relevant for GUT $\mathcal{M}$s (41). The REL mechanism describes the polymer response in the entire velocity interval; in particular, below the excitation-ionization regime, data are consistent with an ~100% contribution from the atomic elastic recoil. This measurement represents an experimental demonstration that the CR39 can effectively record the passage of a $\mathcal{M}$ through the formation of the latent track due to induced atomic elastic recoils.

5. SEARCHES FOR MAGNETIC MONOPOLES

Searches for $\mathcal{M}$s have been performed at accelerators, in cosmic rays, and trapped in matter. There have been no confirmed observations of exotic particles possessing magnetic charge. The limits on the flux of cosmic $\mathcal{M}$s or on the production cross sections at accelerators are usually made

under the assumption of bare magnetic charge. Most of the searches are also sensitive to dyons; by contrast, dedicated analyses are required to search for $\mathcal{M}$s inducing the catalysis of proton decay.

An extensive bibliography on $\mathcal{M}$s dating to the middle of 2011 can be found elsewhere (42, 43). It was intended to consist of nearly all the experimental papers on the subject and only the theoretical papers that have specific experimental implications.

5.1. Searches at Colliders

The possible production of low-mass Dirac $\mathcal{M}$s has been investigated at e^+e^-, e^+p, $p\bar{p}$, and pp colliders, mostly using scintillation counters, wire chambers, and NTDs (44). Searches for monopoles trapped in the material surrounding the collision regions have also been performed.

These searches have set upper limits on $\mathcal{M}$ production cross sections for masses below the TeV scale (**Figure 6**). These limits, based on assumptions of the production processes of monopole–antimonopole pairs, are model dependent.

The highest energies are available in pp collisions at the CERN LHC at a center-of-mass energy of 7 TeV. The ATLAS experiment (45) searched for highly ionizing particles leaving characteristic energy deposition profiles, but found no events. The corresponding upper limit on the cross section at the 95% confidence level (CL) varies from 16 fb to 145 fb for $\mathcal{M}$s with masses between 200 GeV and 1,200 GeV. Early experiments performed at the CERN ISR (46, 47) reported limits in the mass range $\lesssim$30 GeV.

Searches at e^+e^- colliders were based on the detection of $\mathcal{M}$ pairs produced through the $e^+e^- \to \gamma^* \to \mathcal{M}\overline{\mathcal{M}}$ reaction. A search performed with the OPAL detector (48) at the CERN LEP used data collected at a center-of-mass energy of 206.3 GeV (with a total integrated luminosity of 62.7 pb^{-1}); it was based on the measurements of momentum and energy loss in the tracking chambers of the detector. Searches for back-to-back tracks with high-energy release were

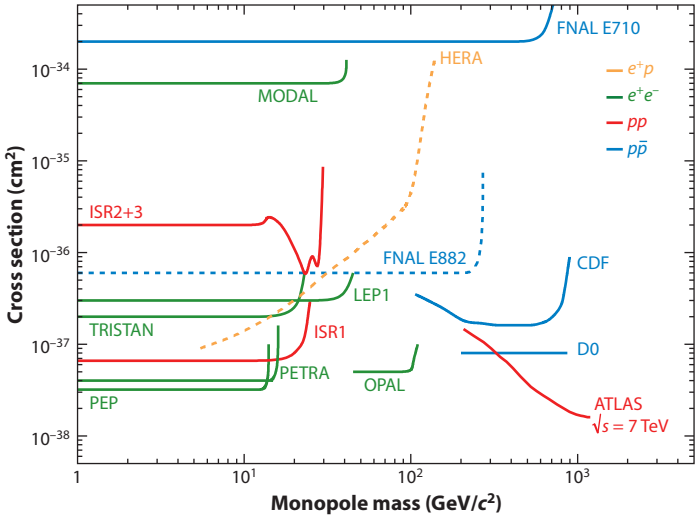

Figure 6

Cross-section upper limits on $\mathcal{M}$ production from searches at colliders. All limits are at 95% CL, except for that of FNAL E882, which is given at 90% CL. The dashed lines represent limits from indirect searches of $\mathcal{M}$ trapped in the beam pipe or detector materials.

conducted in opposite sectors of the jet chamber. The 95%-CL upper limit for the production of monopoles with masses between 45 and 104 GeV was set at 0.05 pb. The MODAL experiment (49) collected data at a center-of-mass energy of 91.1 GeV and an integrated luminosity of ~ 60 nb^{-1}. The detector consisted of a polyhedral array of CR39 NTD foils covering a $0.86 \times 4\pi$ sr angle surrounding the I5 interaction point at LEP. Another experiment (LEP1 in **Figure 6**) searching for highly ionizing particles produced at the OPAL intersection point used a Lexan NTD (50). NTDs around the beam interaction point were also used in earlier searches at e^+e^- colliders, such as the TRISTAN ring at KEK (51), PETRA at DESY (52), and PEP at SLAC (53).

At the Tevatron $\bar{p}p$ collider at Fermi National Accelerator Laboratory (FNAL), the CDF Collaboration (54) searched for $\mathcal{M}$s produced in an integrated luminosity of 35.7 pb^{-1} at a center-of-mass energy of 1.96 TeV. $\mathcal{M}$s would have been detected by the drift chambers constituting the central outer tracker and by the time-of-flight scintillator detectors placed in the 1.4-T magnetic field, parallel to the beam direction. $\mathcal{M}\overline{\mathcal{M}}$ pair production was excluded at 95% CL for cross sections larger than 0.2 pb and monopole masses in the range $200 < M < 700$ GeV. The D0 Collaboration (55) searched for heavy pointlike Dirac monopoles by looking for pairs of photons with high transverse energies. Pairs of nearly real photons can be produced by $\mathcal{M}$s via a particular box Feynman diagram. Finally, NTDs have been used by the FNAL E710 experiment (56).

If produced in high-energy collisions, $\mathcal{M}$s could stop in material surrounding the interaction points of a collider. Discarded parts of the beam pipe or detector material near the interaction regions can be divided into small pieces and passed through a superconducting coil coupled to a SQUID; the signature of the presence of a $\mathcal{M}$ would be the induction of a persistent current in the superconducting loop (10). This method was applied by the H1 Collaboration (57) using the aluminum beam pipe of the HERA lepton–proton collider, which was exposed to a luminosity of 62 ± 1 pb^{-1} at a center-of-mass energy of 300 GeV. The E882 Collaboration (58) also used this technique to search for monopoles trapped in the material surrounding the D0 and CDF collision regions. An initial, preliminary search has already been done using a limited set of available samples. The main purpose of this research (59) was to quantify the expected response of the magnetometer to monopoles, study how fake signals can arise, and run through the protocols needed for a sample release from CERN. A much better-performing search will be carried out when a much larger integrated luminosity at the LHC is collected for material exposed to pp and heavy-ion collisions.

5.2. Direct Searches in the Cosmic Radiation

Direct searches for $\mathcal{M}$s in cosmic rays refer to experiments in which the passage of particles is recorded by detectors under controlled conditions. Several searches for GUT $\mathcal{M}$s have been performed aboveground and underground with different types of detectors (60). $\mathcal{M}$s with masses between 10^5 and 10^7 GeV in the range $\beta \sim 10^{-3} - 10^{-1}$ could reach the Earth's surface from above and be detected, as discussed in Section 3.4. Lower-mass $\mathcal{M}$s may be searched for with detectors located at high mountain altitudes, in balloons, and on satellites.

The background such searches have to contend with is mainly due to muons from the cosmic radiation (61) and natural radioactivity. For this reason, various large detectors have been installed in underground laboratories. The minimum $\mathcal{M}$ mass required in order to reach underground detectors from above (at a given velocity) depends on the overburden of the experiment (62).

$\mathcal{M}$s can be detected in the velocity range $10^{-3} \leq \beta < 1$ through their large ionization energy loss in gaseous detectors, in scintillation counters, or with NTDs. In the velocity range $10^{-4} < \beta < 10^{-3}$, monopoles do not induce ionization in matter (other than via the Drell–Penning effect), although they may still excite atoms, which would emit scintillating light. In all searches performed to date, the cross section for the catalysis process is typically set to

Table 1 Flux upper limits for GUT and IM$\mathcal{M}$s from different experiments[a]

Experiment (reference)	Mass range (GeV/c^2)	β range	Flux upper limit ($cm^{-2}\ s^{-1}\ sr^{-1}$)	Detection technique
AMANDA II upgoing (69)	10^{11}–10^{14}	0.76–1	$(8.8–0.38) \times 10^{-16}$	Ice Cherenkov
AMANDA II downgoing (69)	10^{8}–10^{14}	0.8–1	$(17–2.9) \times 10^{-16}$	Ice Cherenkov
IceCube (71)	10^{8}–10^{14}	0.8–1	$(5.6–3.4) \times 10^{-18}$	Ice Cherenkov
Baikal (68)	10^{7}–10^{14}	0.8–1	$(1.83–0.46) \times 10^{-16}$	Water Cherenkov
ANTARES (70)	10^{7}–10^{14}	0.625–1	$(9.1–1.3) \times 10^{-17}$	Water Cherenkov
MACRO (63)	(5×10^{8})–(5×10^{13})	$>5 \times 10^{-2}$	3×10^{-16}	Scintillator, streamer tube, NTDs
MACRO (63)	$>5 \times 10^{13}$	$>4 \times 10^{-5}$	1.4×10^{-16}	Scintillator, streamer tube
Soudan 2 (66)	10^{8}–10^{13}	$>2 \times 10^{-3}$	8.7×10^{-15}	Gas drift tubes
Ohya (64)	(5×10^{7})–(5×10^{13})	$>5 \times 10^{-2}$	6.4×10^{-16}	Plastic NTDs
Ohya (64)	$>5 \times 10^{13}$	$>3 \times 10^{-2}$	3.2×10^{-16}	Plastic NTDs
SLIM (62)	10^{5}–(5×10^{13})	$>3 \times 10^{-2}$	1.3×10^{-15}	Plastic NTDs
SLIM (62)	$>5 \times 10^{13}$	$>4 \times 10^{-5}$	0.65×10^{-15}	Plastic NTDs
Induction, combined (9)	$>10^{5}$	Any	4×10^{-13}	Induction

[a]Assuming $g = g_D$. Abbreviations: GUT, Grand Unification Theory; IM, intermediate-mass; NTD, nuclear track detector.

very low values (63), equivalent to a null effect in the detector. Searches exploiting the expected catalyzed decays are discussed in Section 5.5.

The most stringent flux upper limits on supermassive $\mathcal{M}$s in the widest velocity range obtained using different experimental techniques were set by the MACRO experiment (63) at the underground Gran Sasso laboratory. This experiment represents a benchmark for $\mathcal{M}$ searches, so we describe it in detail in this section.

Prior to MACRO, excitation and ionization arrays were built on a smaller scale (most during the 1980s) at various locations using a variety of different techniques. Details about these pre-MACRO experiments can be found elsewhere (9). **Table 1** lists searches for bare $\mathcal{M}$s in the cosmic radiation and provides their results.

Figure 7 shows the 90%-CL flux upper limits versus velocity β for GUT $\mathcal{M}$s (with $g = g_D$) from different searches. An experiment performed at the Ohya Mine in Japan (64) used a 2,000-m^2 array of NTDs; another at Baksan in Russia (65) used liquid scintillation counters. Soudan 2 (66), in the United States, was a large, fine-grained tracking calorimeter composed of long drift tubes, and another tracking calorimeter, Kolar Gold Fields (67), was used in India. The other experiments are described in the following subsections.

5.2.1. Searches at a high-altitude laboratory. The SLIM experiment (62) at the Chacaltaya laboratory, 5,230 m above sea level in Bolivia, searched for downgoing IM$\mathcal{M}$s with a 427-m^2 NTD array exposed for 4.2 years to the cosmic radiation. SLIM was sensitive to $\mathcal{M}$s with $g = 2g_D$ in the entire range $4 \times 10^{-5} < \beta < 1$, and with $g = g_D$ for $\beta > 10^{-3}$. No candidate event was observed; a 90%-CL flux upper limit of $\sim 1.3 \times 10^{-15}\ cm^{-2}\ s^{-1}\ sr^{-1}$ was set.

5.2.2. Relativistic magnetic monopoles in neutrino telescopes. Relativistic charged particles traveling through a homogeneous and transparent medium such as water or ice emit Cherenkov radiation that can be detected by arrays or strings of photomultiplier tubes. Baikal (68), AMANDA (69), ANTARES (70), IceCube (71), and the future KM3NeT are usually denoted as neutrino telescopes (72). Due to the Cherenkov mechanism, a huge quantity of visible Cherenkov light would be emitted by a $\mathcal{M}$ with $\beta > c/n = 0.75$, where $n = 1.33$ is the refractive index of

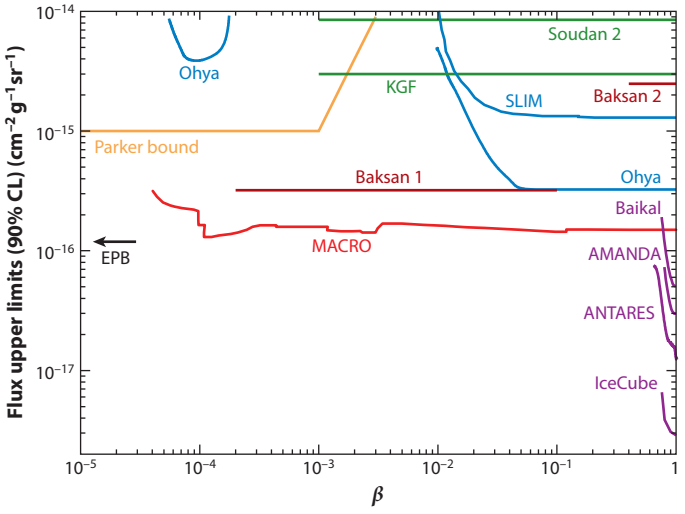

Figure 7

The 90%-CL upper limits versus velocity β for a flux of cosmic GUT $\mathcal{M}$s with magnetic charge $g = g_D$. The Parker bound refers to Equation 8, whereas the extended Parker bound (EPB) refers to Equation 9.

water (73). Additional light is produced by Cherenkov radiation from δ-ray electrons along the monopole's path for velocities down to $\beta = 0.625$.

In most cases, a large background from cosmic muons inhibits searches for downgoing candidates. Upgoing monopoles are required to traverse the Earth before reaching the detector. Note that it is unlikely that GUT supermassive $\mathcal{M}$s could reach (nearly) relativistic velocities. In the IceCube analysis (71), the threshold was adjusted for downgoing signals according to the direction.

5.2.3. Ultrarelativistic magnetic monopoles. Constraints on the flux of ultrarelativistic $\mathcal{M}$s have also been provided by two experiments aimed at detecting radio-wave pulses from the interactions of a primary particle in ice. The Radio Ice Cherenkov Experiment (RICE), consisting of radio antennas buried in the Antarctic ice, set a flux upper limit at 10^{-18} cm^{-2} s^{-1} sr^{-1} (95% CL) for IM$\mathcal{M}$s with a Lorentz factor $10^7 < \gamma < 10^{12}$ and a total energy of 10^{16} GeV (74). The ANITA-II balloon-borne radio interferometer determined a 90%-CL flux upper limit on the order of 10^{-19} cm $^{-2}$ s^{-1} sr^{-1} for a Lorentz factor $\gamma > 10^{10}$ at a total energy of 10^{16} GeV (75).

5.2.4. Induction techniques. Induction detectors are considered the most robust way to identify the passage of a $\mathcal{M}$ of any velocity, mass, and magnetic charge. In searches for $\mathcal{M}$s in cosmic rays, several loops in coincidence are needed to avoid spurious signals. The major drawbacks are the cost of the superconductive loops with the required sensitivity, their small effective area (up to 1 m^2), and the fact that such devices cannot be easily operated in any environment. Several searches using apparata with different numbers of loops (e.g., References 76 and 77) set a combined flux upper limit of $\sim 4 \times 10^{-13}$ cm^{-2} sr^{-1} s^{-1} (out of the scale of **Figure 7**). They provide the only direct constraints on the monopole flux for $\beta < 10^{-4}$.

5.3. The MACRO Experiment at Gran Sasso

MACRO (78) was a large underground detector located in Hall B of Gran Sasso. At Gran Sasso, the minimum thickness of the rock overburden is 3,150 hg cm^{-2} and the cosmic muon flux

is reduced to $\sim 1\ m^{-2}\ h^{-1}$, almost a factor 10^6 lower than at the surface. The detector, which took data with different configurations from 1989 to December 2000, was optimized for the search for GUT $\mathcal{M}$s with velocities in the range $\beta \geq 4 \times 10^{-5}$. The large-area apparatus had global dimensions of $76.6 \times 12 \times 9.3\ m^3$ and $\sim$10,000 m^2sr acceptance to an isotropic particle flux. Redundancy and complementarity were the primary considerations in the experimental design because reasonably very few $\mathcal{M}$s during the detector lifetime were expected. To this end, the apparatus consisted of three independent types of subdetectors: liquid scintillation counters; limited streamer tubes, each with dedicated and independent hardware; and NTDs. MACRO was a multipurpose detector that was able to address different cosmic-ray physics items, such as the disappearance of atmospheric ν_μ, interpreted as due to neutrino oscillations (79).

Because the signature of the passage of a GUT $\mathcal{M}$ across the detector depends strongly on its velocity, different hardware systems were designed and applied to maximize the sensitivity at different velocities. Multiple analysis strategies were adopted in which both the $\mathcal{M}$ signatures and the background characteristics were taken into account. Searches for fast $\mathcal{M}$s were performed in the active detectors via their large energy releases in the liquid scintillator (80) and in the limited streamer tube (81) systems. The background was mainly due to high-energy muons with or without an accompanying electromagnetic shower. Slow $\mathcal{M}$s should leave small signals spread over a wide time window (82); a $\beta \sim 10^{-4}$ monopole should have a time of flight across the detector as long as $\sim$1 ms. This very long transit time implied the use of specific analysis procedures that allowed rejection of the background mainly due to radioactivity-induced hits and possible electronic noise. The final result was obtained via a proper combination of flux upper limits from different searches (63).

5.3.1. The scintillator system. The response of liquid scintillators (discussed in Section 4.2) to heavily ionizing particles was studied experimentally (83), and their sensitivity to particles with velocities down to $\beta \sim 10^{-4}$ was directly measured. Searches for slow $\mathcal{M}$s were performed using dedicated hardware, the slow monopole trigger, and a 200-MHz custom-made wave-form digitizer system (84). The system was sensitive over the entire range of pulse widths and amplitudes (which can be simply a train of single photoelectron pulses lasting several microseconds) expected for slow-moving $\mathcal{M}$s, and it efficiently suppressed narrow (10–50-ns) pulses due to isolated radioactivity and cosmic-ray muons. In addition, the amplitude and time-of-flight information for every particle crossing the counters were recorded by a stand-alone ADC/TDC (analog-to-digital converter/time-to-digital converter) system and used for fast monopole searches.

5.3.2. The limited streamer tube system. The streamer tube system was designed to be effective in the search for $\mathcal{M}$s in a wide velocity range, $10^{-4} < \beta < 1$. For this purpose, a gas mixture containing helium and *n*-pentane was used to exploit the Drell–Penning effect. In the high-velocity region ($\beta > 10^{-3}$), in which the assumptions of the Drell–Penning effect do not apply, the standard ionization mechanism expected for a $\mathcal{M}$ ensures an energy release that is much larger (**Figure 4*b***) than that from minimum ionizing particles. The charge collected on the central wire of the streamer tube has a logarithmic dependence on the energy released inside the active cell, so a charge measurement allows one to distinguish between $\mathcal{M}$s and muons.

5.3.3 The nuclear track detector system. The NTDs covered a total area of 1,263 m^2 and were organized in stacks of $24.5 \times 24.5\ cm^2$, each of which consisted of three layers of CR39,

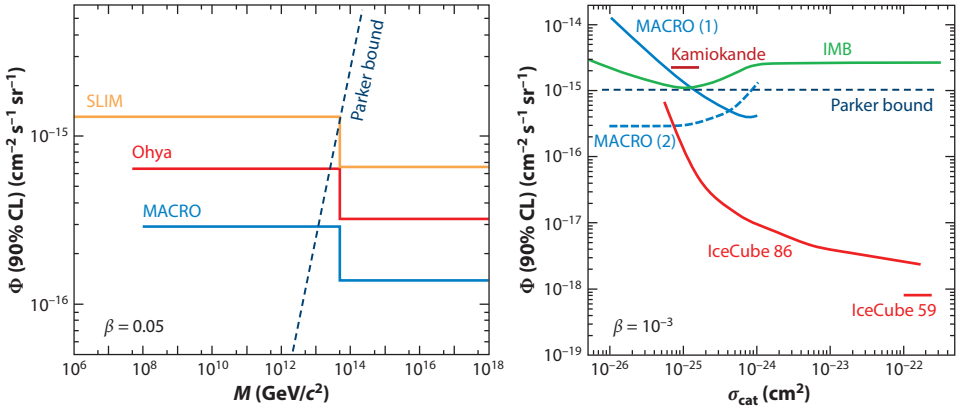

Figure 8

(*a*) Upper flux limits for GUT $\mathcal{M}$s as a function of their mass M for velocity $\beta = 0.05$ as set by MACRO (63), Ohya (64), and SLIM (62). (*b*) Upper limits on the flux of $\beta = 10^{-3}$ $\mathcal{M}$ as a function of the catalysis cross section σ_{cat} for two IceCube analyses (95), two MACRO analyses (92), and analyses by IMB (90) and Kamiokande (91).

three layers of Lexan, and an aluminum absorber placed in an aluminized Mylar bag filled with dry air. The CR39 enabled a search for $\mathcal{M}$s of different magnetic charges and velocity. For a single Dirac charge, the MACRO CR39 was sensitive in the ranges $2 \times 10^{-5} < \beta < 2 \times 10^{-4}$ and $\beta > 1.2 \times 10^{-3}$ (29). Lexan has a much higher threshold, making it sensitive to $\mathcal{M}$s with $\beta > 0.1$. After ~9.5 years of exposure, the top CR39 foils in each stack were etched and analyzed. The searched-for signal was a hole or a biconical track, with the two base cone areas equal within experimental uncertainties. An efficiency close to 100% for finding a signal was achieved. The signature of the passage of a $\mathcal{M}$ was a coincidence among different CR39 layers. Background tracks were induced by proton recoils from neutron interactions or by low-energy nuclei from muon interactions in the material surrounding the apparatus. No signal was found.

5.3.4. The results. No event in MACRO was compatible with the passage of a $\mathcal{M}$ in either individual subsystems or in a combined analysis (85), apart from the so-called spokesman event. That was an LED-induced event (realistically simulating a $\beta \sim 10^{-3}\mathcal{M}$ in the scintillator system) intentionally and secretly generated to test the efficiency of the analyses. Both methods designed to detect a $\beta \sim 10^{-3}\mathcal{M}$ successfully reconstructed the fake spokesman event. **Figure 7** shows the combination of the independent results obtained with the different search methods. **Figure 8*a*** shows the flux upper limits as a function of mass M for monopole velocity $\beta \geq 0.05$ for the MACRO and Ohya underground experiments and for the SLIM high-altitude detector.

5.4. Searches for Monopoles Bound in Matter

Bulk matter could have trapped incident cosmic monopoles over a long exposure time. Several searches for cosmic $\mathcal{M}$s bound in bulk matter have been performed. One technique (86, 87) used few pieces of ~10^9-year-old mica samples, chemically etched and scanned in transmitted light under a microscope, to search for etch pits originating from elastic collisions of a $\mathcal{M}$ with a nucleus. The absence of any etch pit was used to set an upper limit of 10^{-16} to 10^{-18} cm^{-2} s^{-1} sr^{-1} on the flux of supermassive ($M \sim 10^{17}$ GeV) $\mathcal{M}$s with velocities in the range $3 \times 10^{-4} \lesssim \beta \lesssim 1.5 \times 10^{-3}$.

Samples of terrestrial, lunar, and meteoritic materials were passed through a superconducting magnet to search for a persistent current in the coil induced by the monopole after the passage of the samples. For instance, a search for monopoles in polar igneous rocks (88) probed 23.4 kg of samples. Globally, these searches constrain monopole concentrations in matter to below one in a few hundred kilograms, corresponding to an upper limit of the $\mathcal{M}$-per-nucleon ratio of $\sim 10^{-29}$. For a complete review, see section 5 of Reference 33.

5.5. Searches for Monopoles Inducing Catalysis of Nucleon Decay

In the hypothesis of a nonnegligible cross section, the $\mathcal{M}$-induced nucleon decay can be exploited to detect the passage of a monopole through series of decay events (e.g., $\mathcal{M}+p \rightarrow \mathcal{M}+e^{+}+\pi^{0}$ via the Rubakov–Callan mechanism), more or less along a straight line. Early proton decay experiments such as Soudan 1 (89), IMB (90), and Kamiokande (91) searched for cosmic monopoles and established limits to their flux via the catalysis mechanism.

The MACRO Collaboration (92) carried out a dedicated search based on the streamer tube subsystem. A full Monte Carlo simulation of the expected signal was performed. Different catalysis cross sections ranging from 10^{-24} cm^2 to 10^{-26} cm^2 were assumed. The null result of the search was used to set limits on the cross-section parameters and on the $\mathcal{M}$ flux. **Figure 8*b*** shows the upper limits from different experiments for a reference monopole velocity of 10^{-3}.

In neutrino telescopes, Cherenkov light from nucleon decays along the monopole trajectory should produce a characteristic hit pattern. Early results were obtained by the Baikal experiment (93, 94). Recently, the IceCube Collaboration (95) implemented a dedicated slow-particle trigger in DeepCore, the central, dense subdetector of IceCube. The analysis, using 1 year of data, yielded upper limits (90% CL) for the flux of nonrelativistic GUT monopoles at different speeds. The limits (**Figure 8*b***) refer to a velocity of 10^{-3}.

The Super-Kamiokande Collaboration (96) performed an indirect search for GUT monopoles, looking for a neutrino signal coming from proton decay catalyzed by GUT $\mathcal{M}$s captured in the Sun. The flux upper limit was at $\Phi_M(\sigma_0/1\,\mathrm{mb}) < 6.3 \times 10^{-24}(\beta/10^{-3})^2\ \mathrm{cm}^{-2}\,\mathrm{s}^{-1}\,\mathrm{sr}^{-1}$ at 90% CL, assuming a catalysis cross section σ_0 at $\beta = 1$. The limit is valid for $M < 10^{17}$ GeV/c^2.

6. PERSPECTIVES

The Standard Model (SM) explains extremely well all available experimental results obtained in particle physics. The SM predictions have had precise confirmations from measurements performed at increasingly high energy accelerators or colliders, culminating in the discovery at the LHC of the last missing piece of the theory: the Higgs boson. However, most physicists believe that the SM is incomplete and represents a sort of low-energy limit of a more fundamental theory, which should reveal itself at higher energies.

The threshold for this higher-energy limit could be so high that no accelerator on Earth, even in the far future, would be able to reach it. It is in this context that the searches for $\mathcal{M}$s play a fundamental role. Such experiments, as well as those searching for proton decay, motivated the birth of large underground experiments in the 1980s, which contributed significantly to the development of astroparticle physics (97). This field is providing a wealth of new and unexpected results by exploiting the experimental techniques used at accelerators to study the cosmic radiation and in neutrino physics and astrophysics experiments searching for rare phenomena.

In 2015, following a long technical shutdown, LHC will restart data taking. The LHC experiments, all equipped with exceptional detectors, should be able to set new, stringent limits on the

production cross sections for $\mathcal{M}$s. Three complementary techniques have been proposed to search for highly ionizing particles, including classical monopoles in a wide range of magnetic charges: (*a*) in-flight detection in general-purpose apparata, (*b*) in-flight detection using NTDs, and (*c*) the detection of stopped monopoles in matter with the induction technique (98).

The in-flight signature of a monopole event in ATLAS (99) and CMS (100) would be rather striking, yielding a large number of high-threshold hits in the tracker and a very localized energy deposition in the electromagnetic calorimeter (101). New upper limits on the production of exotic particles with masses in the TeV energy range could be set.

MoEDAL (102) aims to detect $\mathcal{M}$s in flight by using NTD stacks deployed around the Point-8 intersection region of the LHCb detector. The array will cover a surface of ~ 25 m^2. Each stack, measuring 25×25 cm^2, consists of nine interleaved layers of CR39, Makrofol, and Lexan NTDs. The $\mathcal{M}$ signature in MoEDAL would be a sequence of collinear etch pits, consistent with the passage of a particle with constant energy loss through all the detector foils. The experiment is expected to be sensitive to monopole production down to cross sections on the order of 1 fb. The sensitivity and redundancy of MoEDAL are enhanced by the addition of a Magnetic Monopole Trapper consisting of an aluminium array. Monopoles stopping within this array could be revealed by the induction technique.

Finally, another indirect search is planned through the analysis of exposed beam-pipe material using SQUIDs. The observability of monopoles and monopolium, the monopole–antimonopole bound state (103), in the $\gamma\gamma$ channel for monopole masses in the range 500–1,000 GeV has been considered elsewhere (104). The interconnection among cosmic-ray studies, neutrino physics, and the search for high-mass $\mathcal{M}$s is also evident in future planned experiments, in which large-area neutrino telescopes and long-baseline neutrino experiments could extend the observation in the space of parameters (M, β) in which monopoles can be sought.

The NOνA detector is designed to study $\nu_\mu \rightarrow \nu_e$ oscillations in the existing Fermilab NuMI neutrino beam. The far detector, with a volume of $15.5 \times 15.5 \times 59.5$ m^3, is located at the surface in northern Minnesota, United States. When completed, this detector will contain $\sim 3.4 \times 10^5$ cells filled with liquid scintillator read out at both ends by avalanche photodiodes. The far detector, due to its surface proximity, large size, good timing resolution, large energy dynamic range, and continuous readout, will be sensitive to the passage of cosmic $\mathcal{M}$s over a wide range of velocities ($10^{-4} < \beta < 1$) and masses. Two dedicated software-based triggers have been designed (105) in order to record fast and slow $\mathcal{M}$ events with high efficiency and a large rejection factor against a rate of cosmic rays of $\sim 10^5$ Hz.

The Iron Calorimeter (ICAL) at the India-Based Neutrino Observatory (INO) is a planned experiment seeking to precisely measure the neutrino oscillation parameters. ICAL will search for $\mathcal{M}$s (106) by using resistive plate chambers (RPCs). The RPCs yield saturated pulses carrying the hit time information, allowing one to track particles crossing the apparatus. The Drell–Penning effect may not be effective in the ICAL gas system; therefore, the experiment would be sensitive to $\mathcal{M}$s with $\beta > 10^{-3}$. The highest allowed velocity is ~ 0.9, limited by the huge background of atmospheric muons. The expected sensitivities of NOνA and ICAL, however, are not significantly larger than that reached by MACRO.

In order to significantly improve upon the existing upper limits on the $\mathcal{M}$ flux, a new generation of experiments covering very large surfaces will be required. These experiments might have on the order of 50- to 100-times-larger acceptance than that of MACRO (and SLIM), on the basis of simple and low-cost detector designs. Achieving this improvement will not be a simple task.

The very large ionization energy losses of $\mathcal{M}$s in a wide velocity range require detectors with high dE/dx thresholds to ease the discrimination of the backgrounds. NTDs are relatively

cheap detectors that can cover very large surfaces. Their disadvantage is that they require chemical etching and optical scanning to extract the signal. Solid-state breakdown counters, which exhibit high-registration dE/dx thresholds, may be a valid alternative to NTDs; they also provide the convenience of electronic registration and simplicity of fabrication, operation, and signal extraction. These properties make such a technique viable for searches for $\mathcal{M}$s and other highly ionizing rare particles (107).

Neutrino telescopes are the largest detectors (with areas of $\sim 10^6$ m^2) that could record a long sequence of hits along a particle trajectory. They can detect relativistic $\mathcal{M}$s that emit radiation above the Cherenkov threshold; alternatively, they can catch the light sequence of a monopole catalyzing proton decay processes. These detectors can reach a sensitivity three orders of magnitudes below the Parker bound, but in a very limited velocity interval or under the assumption of the Rubakov–Callan mechanism.

Recently, several phenomena have been observed in condensed matter as manifestations of the correlations present in strongly interacting many-body systems, behaving as $\mathcal{M}$s (see, e.g., References 108 and 109). These systems are known as emergent particles or quasi-particles. In January 2014, a Dirac monopole quasi-particle in a spinor Bose–Einstein condensate was synthesized. This monopole was obtained by use of an external magnetic field to guide the spins of the atoms forming the condensate (110). The attention attracted by such findings, as well as the many searches performed, searches being planned, and the abundant theoretical literature, demonstrates the persistent interest in the possible existence of the $\mathcal{M}$. Like Dirac, still many people today "would be surprised if Nature had made no use of it" (1, p. 71).

DISCLOSURE STATEMENT

The authors are not aware of any affiliations, memberships, funding, or financial holdings that might be perceived as affecting the objectivity of this review.

ACKNOWLEDGMENTS

We are indebted to Dr. Z. Sahnoun for her valuable help in the preparation of this review. We thank our colleagues from the MACRO and SLIM Collaborations. We acknowledge the contributions of many colleagues in different searches for magnetic monopoles during the past 25 years, in particular S. Balestra, S. Cecchini, M. Cozzi, M. Giorgini, A. Kumar, G. Mandrioli, S. Manzoor, A. Margiotta, V. Popa, M. Sioli, G. Sirri, and V. Togo. The leader of most of those adventures was Giorgio Giacomelli, former MACRO cospokesperson, who passed away on January 30, 2014. To our mentor and deeply missed colleague, this review, largely based on his lessons and reviews, is dedicated.

LITERATURE CITED

1. Dirac PAM. *Proc. R. Soc.* 133:60 (1931)
2. 't Hooft G. *Nucl. Phys. B* 79:276 (1974)
3. Polyakov AM. *JETP Lett.* 20:194 (1974)
4. Lazarides G, et al. *Phys. Rev. Lett.* 58:1707 (1987)
5. Cho Y, Maison D. *Phys. Lett. B* 391:360 (1997)
6. Yang Y. *Proc. R. Soc. Lond. A* 454:155 (1998)
7. Cho YM, Kyoungtae Kimm, Yoon JH. arXiv:1212.3885 [hep-ph] (2012)
8. Preskill J. *Annu. Rev. Nucl. Part. Sci.* 34:461 (1984)
9. Giacomelli G. *Nuovo Cim.* 7:12 (1984)

10. Milton KA. *Rep. Prog. Phys.* 69:1637 (2006)
11. Rajantie A. *Contemp. Phys.* 53:195 (2012)
12. Kibble TWB. *J. Phys. A* 9:1387 (1976)
13. Preskill J. *Phys. Rev. Lett.* 43:1365 (1979)
14. Olive KA, et al. (Part. Data Group) *Chin. Phys. C* 38:090001 (2014)
15. Guth A. *Phys. Rev. D* 23:347 (1981)
16. Kephart TW, Shafi Q. *Phys. Lett. B* 520:313 (2001)
17. Bhattacharjee B, Sigl G. *Phys. Rep.* 327:109 (2000)
18. Julia B, Zee A. *Phys. Rev. D* 11:2227 (1975)
19. Bracci L, Fiorentini G. *Phys. Lett. B* 124:493 (1983)
20. Rubakov VA. *JETP Lett.* 33:644 (1981); Rubakov VA. *Nucl. Phys. B* 203:311 (1982)
21. Callan CG. *Phys. Rev. D* 26:2058 (1982)
22. Arafune J, Fukugita M. *Phys. Rev. Lett.* 50:1901 (1983)
23. Parker EN. *Astrophys. J.* 160:383 (1970)
24. Turner MS, Parker EN, Bogdan TJ. *Phys. Rev. D* 26:1296 (1982)
25. Adams F, et al. *Phys. Rev. Lett.* 70:2511 (1993)
26. Lewis MJ, Freese K, Tarlé G. *Phys. Rev. D* 62:025002 (2000)
27. Kazama Y, Yang CN, Goldhaber AS. *Phys. Rev. D* 15:2287 (1977)
28. Ahlen SP. *Phys. Rev. D* 17:229 (1978)
29. Derkaoui J, et al. *Astropart. Phys.* 9:173 (1998)
30. Agostinelli S, et al. *Nucl. Instrum. Methods A* 506:250 (2003)
31. Bauer G, et al. *Nucl. Instrum. Methods A* 545:503 (2005)
32. Ahlen SP, Kinoshita K. *Phys. Rev. D* 26:2347 (1982)
33. Burdin S, et al. arXiv:1410.1374 [hep-ph] (2014)
34. Eberhard PH, Ross RR, Taylor JD. *Rev. Sci. Instrum.* 46:362 (1978)
35. Cabrera B. *Phys. Rev. Lett.* 48:1378 (1982)
36. Derkaoui J, et al. *Astropart. Phys.* 10:339 (1999)
37. Drell SD, et al. *Phys. Rev. Lett.* 50:644 (1983)
38. Ahlen SP. *Phys. Rev. D* 14:2935 (1976)
39. Cecchini S, et al. *Nucl. Phys. A* 707:513 (2002)
40. Cecchini S, et al. *Nucl. Phys. A* 807:206 (2008)
41. Cecchini S, et al. *Nuovo Cim. A* 109:1119 (1996)
42. Giacomelli G, et al. arXiv:hep-ex/0005041 (2000)
43. Giacomelli G, et al. arXiv:1105.5587 [hep-ex] (2011)
44. Fairbairn M, et al. *Phys. Rep.* 438:1 (2007)
45. Aad G, et al. (ATLAS Collab.) *Phys. Rev. Lett.* 109:261803 (2012)
46. Price MJ. *NATO Adv. Study Inst. B* 111:621 (1983)
47. Giacomelli G, et al. *Nuovo Cim. A* 28:21 (1975); Hoffmann H, et al. *Lett. Nuovo Cim.* 23:357 (1978)
48. Abbiendi G, et al. (OPAL Collab.) *Phys. Lett. B* 663:37 (2008)
49. Kinoshita K, et al. *Phys. Rev. D* 46:R881 (1992)
50. Pinfold JL, et al. *Phys. Lett. B* 316:407 (1993)
51. Kinoshita K, et al. *Phys. Lett. B* 228:543 (1989)
52. Musset P, et al. *Phys. Lett. B* 128:333 (1983)
53. Fryberger D, Coan T, Kinoshita K, Price PB. *Phys. Rev. D* 29:1524 (1984)
54. Abulencia A, et al. *Phys. Rev. Lett.* 96:201801 (2006)
55. Abbott B, et al. (D0 Collab.) *Phys. Rev. Lett.* 81:524 (1998)
56. Bertani M, et al. *Europhys. Lett.* 12:613 (1990)
57. Aktas A, et al. (H1 Collab.) *Eur. Phys. J. C* 41:133 (2005)
58. Kalbfleisch GR, et al. *Phys. Rev. D* 69:052002 (2004)
59. De Roeck A, et al. *Eur. Phys. J. C* 72:2212 (2012)
60. Giacomelli G, Patrizii L, Sahnoun Z. arXiv:1105.2724 [hep-ex] (2011)
61. Cecchini S, Spurio M. *Geosci. Instrum. Methods Data Syst.* 1:185 (2012)
62. Balestra S, et al. *Eur. Phys. J. C* 55:57 (2008)

63. Ambrosio M, et al. *Eur. Phys. J. C* 25:511 (2002)
64. Orito S, et al. *Phys. Rev. Lett.* 66:1951 (1991)
65. Novoseltsev YF, et al. *Nucl. Phys. B* 151:337 (2006)
66. Thron JL, et al. (Soudan 2 Collab.) *Phys. Rev. D* 46:4846 (1992)
67. Krishnaswamy MR, et al. *Phys. Lett. B* 142:99 (1984)
68. Aynutdinov K, et al. *Astropart. Phys.* 29:366 (2008)
69. Abbasi R, et al. *Eur. Phys. J. C* 69:361 (2010)
70. Adrián-Martínez S, et al. (ANTARES Collab.) *Astropart. Phys.* 35:634 (2012)
71. Abbasi R, et al. (IceCube Collab.) *Phys. Rev. D* 87:022001 (2013)
72. Chiarusi T, Spurio M. *Eur. Phys. J. C* 65:649 (2010)
73. Lubsandorzhiev BK. *Nucl. Instrum. Methods A* 553:308 (2005)
74. Hogan DP, et al. *Phys. Rev. D* 78:075031 (2008)
75. Detrixhe M, et al. (ANITA-II Collab.) *Phys. Rev. D* 83:023513 (2011)
76. Huber ME, Cabrera B, Taber MA, Gardner RD. *Phys. Rev. D* 44:636 (1991)
77. Gardner RD, Cabrera B, Huber ME, Taber MA. *Phys. Rev. D* 44:622 (1991)
78. Ambrosio M, et al. *Nucl. Instrum. Methods A* 486:663 (2002)
79. Ambrosio M, et al. *Phys. Lett. B* 434:451 (1998)
80. Ambrosio M, et al. *Astropart. Phys.* 6:113 (1997)
81. Ambrosio M, et al. *Astropart. Phys.* 4:33 (1995)
82. Ambrosio M, et al. *Phys. Lett. B* 406:249 (1997)
83. Ficenec DJ, et al. *Phys. Rev. D* 36:311 (1987)
84. Ahlen S, et al. *Phys. Rev. Lett.* 72:608 (1994)
85. Ambrosio M, et al. *Astropart. Phys.* 18:27 (2002)
86. Price PB, Salamon MH. *Phys. Rev. Lett.* 56:1226 (1986)
87. Ghosh D, Chatterjea S. *Europhys. Lett.* 12:25 (1990)
88. Bendtz K, et al. *Phys. Rev. Lett.* 110:121803 (2013)
89. Bartelt J, et al. *Phys. Rev. D* 36:1990 (1987)
90. Becker-Szendy R, et al. *Phys. Rev. D* 49:2169 (1994)
91. Kajita T, et al. *J. Phys. Soc. Jpn.* 54:4065 (1985)
92. Ambrosio M, et al. *Eur. Phys. J. C* 26:163 (2002)
93. Balkanov VA, et al. *Prog. Part. Nucl. Phys.* 40:391 (1998)
94. Belolaptikov I, et al. *Astropart. Phys.* 7:263 (1997)
95. Aartsen MG, et al. *Eur. Phys. J. C* 74:2938 (2014)
96. Ueno K, et al. (Super-Kamiokande Collab.) *Astropart. Phys.* 36:131 (2012)
97. Spurio M. *Particles and Astrophysics*. Berlin: Springer (2014)
98. De Roeck A, et al. *Eur. Phys. J. C* 72:1985 (2012)
99. Aad G, et al. *J. Instrum.* 3:S08003 (2008)
100. Adolphi R, et al. *J. Instrum.* 3:S08004 (2008)
101. Mermod P. arXiv:1305.3718 [hep-ex] (2013)
102. Acharya B, et al. (MoEDAL Collab.) *Int. J. Mod. Phys. A* 29:1430050 (2014)
103. Hill CT. *Nucl. Phys. B* 224:469 (1983)
104. Epele LN, et al. *Eur. Phys. J. Plus* 127:60 (2012)
105. Wang Z, et al. *J. Phys. Conf. Ser.* 513:012039 (2014)
106. Dash N, Datar VM, Majumder G. arXiv:1406.3938 [physics.ins-det] (2014)
107. Ostrovskiy I, Pinfold J. arXiv:1410.5521 [physics] (2014)
108. Castelnovo C, et al. *Nature* 451:42 (2008)
109. Morris DJP, et al. *Science* 326:411 (2009)
110. Ray MW, et al. *Nature* 505:657 (2014)

Annual Review of Nuclear and Particle Science

Volume 65, 2015

Contents

Index

Errata

An online log of corrections to *Annual Review of Nuclear and Particle Science* articles may be found at http://www.annualreviews.org/errata/nucl